Immiscibility in the Nickel Ferrite-Zinc Ferrite Spinel Binary

SE Ziemniak, AR Gaddipati, PC Sander, SB Rice

Immiscibility in the Nickel Ferrite-Zinc Ferrite Spinel Binary

S. E. Ziemniak

A. R. Gaddipati

P. C. Sander

S. B. Rice

May 2006

Lockheed Martin Corp.
P. O. Box 1072.
Schenectady, New York 12301-1072

ABSTRACT

Immiscibility in the trevorite ($NiFe_2O_4$) - franklinite ($ZnFe_2O_4$) spinel binary is investigated by reacting 1:1:2 molar ratio mixtures of NiO, ZnO and Fe_2O_3 in a molten salt solvent at temperatures in the range 400 - 1000°C. Single phase stability is demonstrated down to about 730°C (the estimated consolute solution temperature, T_{cs}). A miscibility gap/solvus exists below T_{cs}. The solvus becomes increasingly asymmetric at lower temperatures and extrapolates to n - values = 0.15, 0.8 at 300°C. A thermodynamic analysis, which accounts for changes in configurational and magnetic ordering entropies during cation mixing, predicts solvus phase compositions at room temperature in reasonable agreement with those determined by extrapolation of experimental results. The delay between disappearance of magnetic ordering above T_C = 590°C (for $NiFe_2O_4$) and disappearance of a miscibility gap at T_{cs} is explained by the persistence of long-range ordering correlations in a quasi-paramagnetic region above T_C.

Zinc treatment, in which trace (ppb) levels of Zn(II) ions are maintained in the coolant of light water reactors, is an effective means to minimize the corrosion of, and cobalt activity pickup on, NiCrFe alloys used to define the reactor coolant circuit [1]. In response to mixing limitations in the $(Ni, Fe)(Fe_{1-n}Cr_n)_2O_4$ spinel binary, non-selective oxidation of these alloys results in the formation of a duplex corrosion oxide layer; each layer representing a solvus phase in the immiscible ferrite-chromite binary. The benefits of zinc treatment are known to be concentration dependent and analyses of the corrosion oxide layers indicate that substitution/replacement of Fe(II) ions by Zn(II) is occurring in both solvus phases [2].

Consistent with the tetrahedral site preference of the Zn(II) ion and the availability of tetrahedral sites in the inner, chromite-rich solvus, no mixing limitations are expected when the thermodynamic equilibrium for this zinc substitution reaction is considered. On the other hand, the outer, ferrite-rich solvus possesses an inverse spinel lattice in which the Fe(II) ions being replaced are located in octahedral, rather than tetrahedral sites. Although the ferrite-based layer is usually considered non-protective with regard to minimizing corrosion, zinc treatment causes morphological/structural changes in this layer that may increase its protectivity [2]. That is, mixing limitations on divalent cation constituents in ferrite spinel binaries may play a role in explaining the effects of zinc treatment.

The appropriate ferrite binaries for modeling the outer corrosion layer on NiCrFe alloys are Fe_3O_4-$ZnFe_2O_4$ and $NiFe_2O_4$-$ZnFe_2O_4$. Presently, only indirect evidence exists regarding the existence of a consolute solution temperature (T_{cs}) and solvus phase compositions in the

magnetite (Fe_3O_4) - franklinite ($ZnFe_2O_4$) binary. For example, naturally-occurring mineral

deposits of franklinite are observed to contain exsolution lamellae of magnetite within the

franklinite phase [3]. Graydon and Kirk [4] have concluded that the exsolution texture is

consistent with the existence of a miscibility gap and tentatively fixed the critical solution point

at 800°C, $n_1 = n_2 = 0.2$. In addition, application of a spinel mixing model [5] predicts T_c . 430°C

and $n = 0.1, 0.7$ at 300°C. On the other hand, experiments conducted at 500°C have been

unsuccessful in demonstrating immiscibility in the $(Fe_{1-n}Zn_n)Fe_2O_4$ binary [6]. Similarly,

experimentally-based Gibbs energies of mixing in the $(Ni_{1-n}Zn_n)Fe_2O_4$ binary demonstrate only

single phase behavior at 700°C [7].

Based on our successful application of a molten salt method for investigating trivalent ion

mixing in the $Ni(Fe_{1-n}Cr_n)_2O_4$ spinel binary [8], this method is again employed to investigate

divalent cation mixing in the $(Ni_{1-n}Zn_n)Fe_2O_4$ spinel binary.

EXPERIMENTAL

Immiscibility in the trevorite ($NiFe_2O_4$) - franklinite ($ZnFe_2O_4$) binary was investigated by

reacting 1:1:2 molar ratio mixtures of NiO, ZnO and Fe_2O_3 in a molten salt solvent at

temperatures in the range 400-1000°C. The existence of multiple spinel phases was detected

using a combination of X-ray diffraction (XRD) and energy dispersive X-ray spectroscopy

(EDX) on an analytical electron microscope (AEM).

Each synthesis began by dry-mixing the reagent grade powders in excess quantities of various

LiCl/KCl salt mixtures. Mixing was accomplished by tumbling with zirconia balls in a plastic

bottle. After the pre-mixing operation was completed, the powder mixture was poured into a

platinum crucible, covered with a platinum lid and placed in an air furnace. Five spinel

formation periods were tested, see Table 1; the first being conducted in the single phase region to

demonstrate adequacy of the spinel synthesis route. Compositions of the solvent salt mixtures

were selected as a compromise between melting point and the need for low vapor pressure at test

temperature. Despite these precautions, approximately 20% of the solvent salt evaporated during

the spinel formation period.

Upon removal from the furnace, each reacted oxide-salt mixture was dissolved in deionized

water and the spinel oxide product was recovered by filtration. The oxide product was

thoroughly washed to remove all traces of chloride, rinsed with isopropanol and dried. This

synthesis produced an extremely fine-grained oxide powder, see Fig. 1. These SEM images

reveal that the microcrystals possess an octahedral habit and range in size between 0.2 and 0.5

$\digamma$m.

Powder XRD analyses were performed using a Rigaku Dmax B system equipped with a

diffracted-beam graphite monochromator. Copper K$_\bullet$ radiation (δ_1 = 1.54956 D, δ_2 = 1.54439

D) was used; step size was 0.024°. A tungsten internal standard was included in each analysis to

ensure highly accurate 2θ measurements. Microchemical analyses of individual crystal grains

were performed using an Oxford Inca EDX detector on a JEOL 2010F field emission AEM in

scanning mode, with Cliff-Lorimer thin film data reduction to produce semi-quantitative results.

RESULTS

A.   Unit Cell Dimensions of the Spinel Phases

Powder XRD analyses of the reaction products from Runs 2-5 revealed the presence of two

spinel oxides (i.e., cubic phases) having broad diffraction peaks, along with trace to minor

amounts of unreacted NiO and Fe_2O_3. Run 1 was an exception, since only a single spinel phase

was present and the solid phase had rather narrow diffraction peaks, ~0.2° full width at half

maximum (FWHM).

Fig. 2 plots the results of spectral deconvolutions of the [8, 4, 4] spinel peak from the above

reaction products. Note that doublet peaks are observed for the tungsten standard because

copper K_α radiation has two wavelengths, i.e., $K_{\alpha 1}$ and $K_{\alpha 2}$, which are readily distinguishable at

large 2θ values.

Lattice parameters for the cubic spinel phases, as determined from a whole pattern fit of XRD

peak positions found for five high angle reflection planes: [6, 6, 4], [9, 3, 1], [8, 4, 4], [10, 2, 0]

and [9, 5, 1] are compared in Table II. Also included in Table II are the full widths at half-

maximum (FWHM) of the [8, 4, 4] peak. The slightly higher FWHM for the second spinel phase

relative to the first may be an artifact of the fitting procedure, since the fit includes the [4, 2, 2]

peak from any unreacted NiO that occurs at $2\theta \approx 129°$. This omission is expected to have a

negligible effect on the calculation of unit cell dimension since the whole pattern fit includes

four other peaks unaffected by NiO and only minor/trace amounts of NiO were detected.

Finally, unit cell dimensions (a_o) were interpreted to give *n*-values in the $(Ni_{1-n}Zn_n)Fe_2O_4$ spinel

binary by application of a calibration curve constructed from room temperature lattice parameter

measurements for single-phase trevorite-franklinite solid solutions of known composition [9], see Fig. 3. Subsequent, independent investigations [10, 11] confirm the accuracy of the calibration curves to better than 0.001 C. The n-values determined in this manner are summarized in the sixth column of Table II.

Based on the chemical compositions of the ferrite phases to be reported, wherein small amounts of Fe^{3+} reduction were indicated, it was necessary to adjust the calibration curve to account for the presence of Fe^{2+} in the ferrites. A revised calibration curve was constructed by interpolation between the original lattice parameter curve for the trevorite-franklinite binary and that for the magnetite-franklinite binary [11] based on the fractions of Fe^{2+} reported in Table III. The bias-corrected n-values are given in parentheses in the sixth column of Table II.

Due to the asymmetric nature of the solvus and the smaller difference in composition between the zinc-rich solvus (n_1) and the equivalent (single phase) composition of the reactant mixture, i.e., $n = 0.5$, lesser amounts of the nickel-rich solvus (n_2) were present at 700°C than in other syntheses at lower temperatures (see Fig. 2d). Therefore, less precise estimates of n_2 were obtained at 700°C, since only three high angle peaks (rather than five) could be deconvoluted for lattice parameter determination. To provide an internally consistent estimate for n_2 in Run 2, n_2 was recalculated via material balance using the more accurate n_1 value and the equivalent single-phase spinel composition of the reactants assuming complete conversion ($n = 0.5$). The n_2 values recalculated in this manner are summarized in the final column of Table II.

B.   <u>Spinel Phase Composition (Microchemical Analyses)</u>

Microchemical analyses performed concurrently with the Fig. 1 SEM examinations (i.e., EDX) confirmed that the reaction product crystals contained the expected elements (O, Fe, Ni and Zn). Initial attempts to quantify metal ion compositions of individual microcrystals by analysis of polished, epoxy mounts using an electron microprobe proved unsuccessful due to the small crystal sizes and penetrating nature of the probe. A more satisfactory preparatory method was subsequently developed, which involved application of an ultrasonic step prior to dispersing the sample, in powder form, onto a grid. This sample preparation method allowed more refined characterization of individual crystal grains using EDX in the AEM, since interferences due to overlap were minimized. Beam spot size for these microchemical analyses was ~0.2 nm.

Figure 4 plots the results obtained from AEM/EDX analyses of more than 100 different, individual particles from each synthesis which were judged to be single crystals. (Only about 50 microcrystals from Run 1 were analyzed.) To facilitate comparisons with the trevorite-franklinite spinel binary $(Ni_{1-n}Zn_n)Fe_2O_4$, iron content is plotted as the ordinate, while the abscissa is defined as at% Zn/(at% Zn + at% Ni) and the metals contents is normalized to unity: at% Zn + at% Ni + at% Fe = 100. Lines drawn through the data points represent the results of linear, least-squares fits, see Table III. As expected, spinel iron fractions are approximately 2/3 in Runs 1 and 2, but the nickel-rich solvus in Runs 3-5 tends toward higher iron fractions, indicating that significant levels of Fe^{2+} are present. Also, as expected in Runs 2-5, compositions of the microcrystals separated into two groups, one with Ni > Zn, the other with Ni < Zn; each group having a rather wide range in Ni – Zn composition. As an initial approximation, mean values of composition (n), normalized to the $(Ni_{1-n}Zn_n)Fe_2O_4$ binary, were determined for each group. The mean n-values, depicted by arrows in Fig. 4 and summarized in

Table III, tended to separate as temperature decreased, in general agreement with the compositional changes inferred from the XRD results.

The measured spread in composition of the microcrystals created in Runs 3 and 4 was so great that data overlap prevented determination of an average composition for each solvus phase. The cause of the somewhat excessive spread in n-values within each solvus phase was investigated by constructing nanometer-scale composition maps in the AEM for select single microcrystals synthesized at 700 (Run 2) and 500°C (Run 4), see Figs. 5 and 6. Results for Run 2, where two compositional groupings were discernable, were as expected: individual microcrystals had a uniform composition; some had Zn > Ni, some had Zn < Ni. On the other hand, the Run 4 results revealed that each solvus was not present as an individual microcrystal having an average (homogeneous) composition. Rather, each microcrystal itself was separated into ferrite regions that were either zinc-rich or nickel-rich. Compositional zoning is indicative of incomplete phase separation, due to insufficient time and lower rates of ionic diffusion at the lower test temperatures. Therefore, the excessive spread in n-results for Runs 3-5 was probably due to analysis of overlapping regions having different compositions and inability to position the probe beam so that each solvus composition would be isolated. Based on the composition map constructed for a microcrystal from Run 4 (500°C, see Fig. 6), the nickel-rich solvus composition, $n_1 = $ Zn/(Zn + Ni), was 0.13, while the zinc-rich solvus had $n_2 = 0.83$. Figure 7 plots the solvus determined for the $(Ni_{1-n}Zn_n)Fe_2O_4$ spinel binary based on the XRD (Table II, columns 6 and 7) and AEM/EDX (Table III) results.

INTERPRETATION OF RESULTS

Mixing in spinel binaries is expected to follow from a thermodynamic model of cation disordering, refined previously [12] and applied to mixing in the $Fe(Fe_{1-n}Cr_n)_2O_4$ system. Without solving the model equations to determine cation disordering as functions of temperature and thereby $)G_{mix}(T)$, it is possible to characterize the source of immiscibility by analyzing each of the modeling terms that contributes to the entropy of mixing at room temperature:

$$\Delta S_{mix} = \Delta S_c + \Delta S^{mag} + \Delta S^{el} \tag{1}$$

The first term $()S_c)$ arises from changes in configurational entropy and deals with how the cations are distributed between octahedral and tetrahedral sites in the spinel lattice. The second term $()S^{mag})$ deals with a magnetic ordering contribution to entropy which is prevalent in spinels containing iron cations. This phenomenon arises because the moments, *i.e.*, spins, of the tetrahedral Fe^{3+} ions tend to align antiparallel to the moments of the octahedral Fe^{3+} (and Fe^{2+}) ions, resulting in a type of magnetism known as ferrimagnetism [13]. The third term arises from changes in electronic entropy, which is possible for transition metal cations because they possess an incomplete 3d shell of electrons. These electrons may be stabilized by placement in an octahedral versus a tetrahedral (crystal) field, such as exists in a spinel lattice. Given the present three cations, S^{el} is zero for Zn^{2+} and Fe^{3+}, while it is a maximum for Ni^{2+} (R ln 3, see [5]).

A.   Calculation of $)S_c$

Previously we demonstrated how the Temkin equation was applied to calculate configurational entropy (S_c) from cation distributions obtained from M˘ssbauer and XRD lattice parameter analyses of a single phase spinel binary. Based on the availability of these analyses for the $(Ni_{1-n}Zn_n)Fe_2O_4$ binary [9-11], it is known that the cations are distributed according to:

Ion	Tet (A)	Oct (B)	Sum
Ni^{2+}	0	1 - n	1 - n
Zn^{2+}	n	0	n
Fe^{3+}	1 - n	1 + n	2
Sum	1	2	3

In other words, Ni^{2+} ions are confined solely to octahedral sites, while Zn^{2+} ions are located only on tetrahedral sites. Application of the Temkin formula [14] gives

$$-S_c / R = n \ln n + 2(1-n) \ln(1-n)$$
$$+ (1+n)\ln(1+n) - 2 \ln 2 \tag{2}$$

The entropy of mixing is determined by subtracting the mole fraction weighted configurational entropies of the end member spinels from S_c of the mixture. Substitution of the cation distribution for a normal spinel, $ZnFe_2O_4$ ($n = 1$), gives $-S_c/R = 0$, while the inverted configuration of $NiFe_2O_4$ ($n = 0$) gives $-S_c/R = -2 \ln 2$, so

$$-\Delta S_c / R = n \ln n + 2(1-n) \ln (1-n)$$
$$+ (1+n) \ln (1+n) - 2n \ln 2 \tag{3}$$

A necessary consequence of the above cation distribution is that $\rangle S^{el} / 0$, since the Ni^{2+} and Zn^{2+} cations do not move between octahedral and tetrahedral sites. Fig. 8 shows that the calculated entropies of mixing, based solely on changes in configurational entropy, are much greater than those calculated by the ideal mixing formula:

$$-\Delta S_{mix}^{ideal}/R = n \ln n + (1-n) \ln (1-n) \tag{4}$$

More importantly, however, near-symmetry in the $\rangle S_c/R$ plot about n . 0.55 precludes the existence of inflection points, indicative of immiscibility. It is noteworthy that this result differs from that found for trivalent cation mixing in the $Ni(Fe_{1-n}Cr_n)_2O_4$ spinel binary [8]. Here $\rangle S_{mix}$

11

was dominated by the $\mathbf{)}\,\mathrm{S_c}$ term, which was highly asymmetric and contributed significantly to immiscibility.

B.   Calculation of $\mathbf{)}\,\mathrm{S^{mag}}$

Since loss of magnetic ordering is indicated by an anomaly, *i.e.*, a sharp decrease, in heat capacity (C_p°) at the transition temperature (T_N or T_C), the contribution to entropy may be estimated by resolving the temperature functionality of C_p° into magnetic and non-magnetic (*i.e.*, lattice-vibrational) contributions and performing the proper integrations to obtain S^{mag}. Previously, we demonstrated how magnetic entropy for one of the end-member spinels could be extracted from high-temperature heat capacity measurements of nickel ferrite [15]. Briefly, the methodology relies on infrared spectroscopic measurements to define the lattice-vibrational (baseline) contribution to heat capacity and then fits the excess as the sum of a spin wave component and an empirical, Inden-type model. It was also necessary to include a (fitted) correction factor to account for the small difference between C_P and C_V which causes C_P to exceed the $C_V = 21R$ high temperature limit, see Eq. (12).

Spin wave analysis for nickel ferrite yields four terms:

$$C_V^{mag,sw} / R = F(\omega_1) + F(\omega_2) + \mathrm{E}\left(\frac{12 J_{AB} s_A}{kT}\right) + \frac{1}{3}\mathrm{E}\left(\frac{24 J_{AB} s_B}{kT}\right) \tag{5}$$

where

$$F(\omega_1) = \frac{1}{4\pi^2}\left(\frac{kT}{Z}\right)^{3/2} \int_o^\infty \frac{x^{5/2} e^x}{\left(e^x - 1\right)^2} dx = \frac{1}{4\pi^2}\left(\frac{kT}{Z}\right)^{3/2} (4.4578) = 0.1129 \left(kT/Z\right)^{3/2} \tag{6}$$

$$F(\omega_2) = \frac{1}{4\pi^2}\left(\frac{kT}{Z}\right)^{3/2}\int_\phi^\infty \frac{x^2 e^x (x-\phi)^{1/2}}{(e^x-1)^2}dx \qquad\qquad (7)$$

$$\phi = \frac{12 J_{AB}(2s_B - s_A)}{kT} \qquad \text{and} \qquad Z = \frac{11 J_{AB} s_A s_B}{2(2s_B - s_A)} \qquad (8, 9)$$

and s_A and s_B are the average spins associated with the ionic moments at the tetrahedral (A) and octahedral (B) sites, E(arg) represents the dimensionless Einstein function and J_{AB} is the A-B exchange interaction (treated as a fitted parameter).

The Inden model is applied in the form of a three-term-truncated power series written in terms of dimensionless temperature, $\tau = T/T_C$ [16] :

$$C_V^{mag,\lambda} = 2K^- R\left(\tau^m + \frac{1}{3}\tau^{3m} + \frac{1}{5}\tau^{5m}\right) \qquad (\tau < 1) \qquad (10a)$$

$$C_V^{mag,\lambda} = 2K^+ R\left(\tau^{-n} + \frac{1}{3}\tau^{-3n} + \frac{1}{5}\tau^{-5n}\right) \qquad (\tau > 1) \qquad (10b)$$

where K^-, m, K^+ and n are fitted parameters and $T_C = 858$ K. The resulting model parameters are summarized in Tables IV (baseline) and V (magnetic). The fitted heat capacities and magnetic contribution to heat capacity for $NiFe_2O_4$ are shown in Figs. 9 and 10, respectively.

$ZnFe_2O_4$, in contrast to $NiFe_2O_4$, is a normal spinel that loses its antiferromagnetism (AFM) in an asymmetric λ-transition at 9.5 K. The transition temperature is known as the Neel temperature, because beyond this point, the magnetic susceptibility of zinc ferrite remains relatively flat and

does not decrease in conformance with the Curie-Weiss law until after the paramagnetic Curie temperature is reached. The latter occurs in the vicinity of 40 K. Progress in reconciling theory with experiment in the low temperature region, *i.e.*, T < 50 K, has been slow because the shape of the λ-type anomaly has been found to be sensitive to sample preparation, *i.e.*, dependent on stoichiometry, thermal processing and crystal/grain size (see Refs. [17 - 19]).

Recent work by Vologin [18] has interpreted the effects of stoichiometry and impurities on the basis of a degenerate antiferromagnetic state in which the ground state is determined by sample quality. More importantly, however, new heat capacity measurements were reported for a single crystal of stoichiometrically-pure $ZnFe_2O_4$. The new values are virtually identical to those previously reported by Westrum and Grimes [17] for T > 15 K, but are significantly higher at lower temperatures. Furthermore, the observed trend of increasing heat capacity with nanocrystal size in the antiferromagnetically-ordered region reported by Ho et al. [19] is also consistent with the measurements of Vologin. These results indicate that the heat capacities reported by Westrum and Grimes are too low in the AFM region. Therefore, only the measurements reported by Vologin were considered when modeling C_P below 15 K. (Note that an apparent error exists in the zinc ferrite heat capacities plotted in Fig. 1 of Vologin [18]: it is necessary to multiply the reported values of C_V/RT by a factor of 7.6 in order to reproduce the values reported by Westrum and Grimes [17].)

Since the available database on zinc ferrite heat capacities cover a rather limited temperature range from 4.5 to 345 K, the conversion between C_P and C_V was estimated by applying the thermodynamic relationship

$$C_P - C_V = TV\alpha^2/\kappa \tag{11}$$

where the properties molar volume (V), linear expansivity (α) and isothermal compressibility (κ) were taken from Grimes [20]. The values calculated by the above equation were then fitted to a quadratic dependence in temperature:

$$C_P/C_V = 1 + \gamma_1 T + \gamma_2 T^2 \tag{12}$$

In $ZnFe_2O_4$, only two Fe^{3+} ion pairs of each six nearest-neighbor pairs have antiparallel spins; spins in the four remaining pairs of each primitive cell are orthogonal. Thus 2/3 of the antiferromagnetic exchange bonds in zinc ferrite exhibit "topological frustrations"[21], since they do not result in spins that are exactly antiparallel. In such a system, AFM at the spinel octahedral positions is degenerate [22], and to a first approximation, thermal population of the levels is governed by Maxwell-Boltzmann statistics. This allows the magnetic component to heat capacity to be represented as a Schottky anomaly [18]:

$$\frac{C_V^{mag,sw}}{R} = \frac{g\left(\Delta/T\right)^2 exp\left(\Delta/T\right)}{\left[1 + g \ exp\left(\Delta/T\right)\right]^2} \tag{13}$$

where g relates to the relative degeneracy of the ground and excited levels and Δ is the split between energy levels. Presently, both were treated as fitting parameters. It is noted that in the high temperature limit, Eq. (13) provides magnetic heat capacities that reduce to zero with a T^{-2} tail. According to the analysis of Tachiki and Yosida [23], the limiting magnetic heat capacity per Fe^{3+} ion is given in terms of the exchange integral (J_{BB}) as

$$C_V/k = 4/3 \ (J_{BB}/k)^2 s_B^2 (s_B + 1)^2 \ T^{-2} \tag{14}$$

where $s_B = 5/2$.

The magnetic heat capacity analysis for $ZnFe_2O_4$ is completed by including the Indel model, Eq. (10), to fit excess portions of the thermal anomaly not accounted for by Eq. (13). Fig. 11 compares the fitted and measured C_p for franklinite based on the parameters provided in Tables IV and V; magnetic contribution to heat capacity is shown in Fig. 12. It is noteworthy that a small Schottky "bump", attributed to a vibrational anomaly of octahedral Fe^{3+} ions, is observed around $80 - 85$ K in both ferrites [15, 20], see Table IV. Finally, the magnetic contribution to entropy for $NiFe_2O_4$ and $ZnFe_2O_4$ is determined by integration:

$$\Delta S^{mag}\left(\infty\right) = \int_0^\infty \left(C_P^{mag}/T\right)dT \qquad (15)$$

In this manner, it is found that $\mathbf{)}\,S^{mag}(\infty)/R = 4.121$ and 3.160 for nickel ferrite and zinc ferrite, respectively.

Although heat capacity measurements are available for the $(Ni_{1-n}Zn_n)Fe_2O_4$ spinel binary at intermediate values of $n = 0.2, 0.4, 0.6$ and 0.8 [26], their frequency in the λ-transition region is insufficient to permit the magnetic contribution to heat capacity to be extracted in the same manner as done for the end-members ($n = 0$ and 1). This difficulty was overcome by approximating the shapes of the end-member magnetic entropy curves, defined as

$$\sigma_n^{mag}(T) = S_n^{mag}(T) - \mathbf{)}\,S_n^{mag}(\infty) \qquad (16)$$

by the polynomial

$$\ln\left|-\sigma_n^{mag}(T)/R\right| = d_n + e_n\,T^3 \qquad (17)$$

where the d_n coefficients were constrained to give the $T = 0$ intercept, i.e., $d_n = \ln\mathbf{)}\,S_n^{mag}(\infty)/R$, and the e_n coefficients were related to the Curie temperatures for solid solutions in the $(Ni_{1-n}Zn_n)Fe_2O_4$ spinel binary. The composition dependency of $\mathbf{)}\,S^{mag}(\infty)$ was modeled by linearly interpolating between end-member values

$$) S_n^{mag}(\infty)/R = 3.160\, n + 4.121\, (1-n) \qquad (18)$$

while the measured Curie temperatures [9] were fitted to a third order Redlich-Kister polynomial:

$$T_C(n) = 10n + 863(1-n) + 349.5n(1-n) + 105.2n(1-n)(2n-1) \qquad (19)$$

Estimated Curie temperatures deviated from the measurements of Leung *et al.* [9] by ± 4 K (1**F**) and by less than 16 K from the results of Landiya *et al.* [26]. The interpolation process was completed based on the assumption that the product $e_n T_C^3$ varied linearly with n between the fitted end-member values of $e_0 = -4.907\ 10^{-4}$ ($T_N = 9.5$ K) and $e_1 = -2.936\ 10^{-9}$ ($T_C = 858$ K). As shown in Fig. 13, the magnetic contribution to entropy in the $(Ni_{1-n}Zn_n)Fe_2O_4$ binary is negligible at room temperature for solids having n >0.7 and for all solids above 1000°C.

Changes in magnetic entropy upon mixing are readily determined from

$$\Delta S^{mag} = S^{mag}(n) - nS^{mag}(n=1) - (1-n)S^{mag}(n=0) \qquad (20)$$

Figure 14 plots the results of these calculations at room temperature. Two trends are noteworthy: (1) for $n < 0.6$,) S^{mag} is nearly equal in magnitude to) S_c but opposite in sign (see Figs. 5, 14), and (2) for $n > 0.6$,) S^{mag} changes sharply with n and becomes very small at n-values between 0.75 and 1.0.

C.   Calculation of) S_{mix} (298)

Summation of) S_c (Fig. 8) and) S^{mag} (Fig. 14) produces the sought-after) $S_{mix}(n)$ curve for the $(Ni_{1-n}Zn_n)Fe_2O_4$ binary at room temperature. Figure 15 shows that the curve possesses two local minima which is indicative of the existence of a solvus. Construction of a common tangent line between the two minima provides composition estimates of n . 0.13 and 0.78 for the two solvus

phases. These estimates, shown as arrows on a plot of the experimentally determined solvus, are seen to be in reasonable agreement with extrapolation of the high temperature data to room temperature. Thus, $)H_{mix}$ is not expected to contribute significantly to immiscibility.

SUMMARY/CONCLUSIONS

Mixing in the trevorite-franklinite binary $(Ni_{1-n}Zn_n)Fe_2O_4$ has been investigated using a molten salt technique over the temperature range 400 - 1000°C. A consolute solution point has been found to exist at 730°C, $n_1 = n_2 = 0.4$. A miscibility gap exists below this point and extrapolates to $n = 0.15, 0.8$ at 300°C. At temperatures slightly below the consolute solution point individual microcrystals of each solvus phase were produced which had homogeneous compositions. At temperatures < 500°C, the time-temperature conditions were insufficient to cause complete phase separation, and compositional zoning was observed within individual microcrystals. The latter phenomenon was also accompanied by the preferential appearance of small quantities of Fe(II) in the nickel-rich ferrite phase. It is noteworthy that corrosion testing of an FeCrNi alloy in zinc-treated water near 300°C [2] yielded ferrite-based oxide crystals $(Fe, Ni)_{1-n}Zn_nFe_2O_4$, $n \sim$ 0.05 having a smaller size (~20 nm) than those synthesized in the present experimental program, even though the outer layer ferrite crystals closest to the metal oxide-water interface were much larger (~0.1-0.5 µm) and had a higher zinc content ($n \sim 0.6$).

The magnetic ordering contribution to entropy for nickel ferrite and zinc ferrite was extracted from an anomaly in the heat capacity curves that occur at the respective Curie and Néel temperatures. By fitting the anomaly as the sum of a theoretical component (spin wave or Schottky) and an empirical component (Inden model), it was possible to account for magnetic

ordering in a quasi-paramagnetic region above T_C. The latter is believed to explain why the consolute solution temperature (point at which immiscibility first occurs) is greater than the Curie temperature (point at which long-range magnetic ordering disappears) in their binary solid solutions. A thermodynamic analysis of entropy changes during mixing, which accounted for configurational (octahedral vs. tetrahedral sites), magnetic ordering (spin alignment between tetrahedral Fe^{3+} and octahedral Fe^{3+}/Fe^{2+} ions) and electronic (crystal field stabilization) changes, revealed that immiscibility is caused primarily by changes in magnetic ordering entropy. This result differs from that found previously for mixing of trivalent cations in a spinel binary [12], where changes in both configurational and magnetic ordering entropies contributed to immiscibility.

Since Fe_3O_4, $NiFe_2O_4$ and $CoFe_2O_4$ are inverse spinels that possess Curie temperatures in excess of 530°C [9, 27], it is concluded that each will form a binary solid solution with $ZnFe_2O_4$ that will exhibit a miscibility gap above 530°C but below 700-750°C. This conclusion is consistent with the present results for the $NiFe_2O_4$-$ZnFe_2O_4$ binary, estimates for the Fe_3O_4-$ZnFe_2O_4$ binary [4] and exsolution behavior observed in the $CoFe_2O_4$-$ZnFe_2O_4$ binary at 700°C [28].

Future modeling effort remains. Refined estimates of cation disordering need to be obtained at elevated temperatures for the end member spinels ($NiFe_2O_4$ and $ZnFe_2O_4$) and their spinel binary using a model similar to that developed to predict cation disordering in the Fe_3O_4-$FeCr_2O_4$ spinel binary [12]. This work will provide temperature functionalities for disordering and allow mixing model predictions to be made at elevated temperatures.

REFERENCES

1.   C. J. Wood, Developments in water chemistry of nuclear power reactors, in "Water Chemistry of Nuclear Reactor Systems 8", (British Nuclear Energy Society, London, 2000) pp. 1-6

2.   S. E. Ziemniak, M. Hanson, Zinc treatment effects on corrosion behavior of 304 stainless steel in high temperature, hydrogenated water, Corros. Sci. (MS 2369, in press)

3.   E. A. J. Burke, C. Kieft, Franklinite from Langban, Sweden, a new occurrence, Lithos 5 (1972) 69-72

4.   J. W. Graydon, D. W. Kirk, The evidence for a miscibility gap in the Fe_3O_4 - $ZnFe_2O_4$ system – a review, Met. Trans. 19B (1988) 919-925

5.   H. St. C. O'Neill, A. Navrotsky, Cation distributions and thermodynamic properties of binary spinel solid solutions, Amer. Mineral. 69 (1984) 733-753

6.   A. J. Valentino, C. B. Sclar, Experimental study of the magnetite ($FeFe_2O_4$) – franklinite ($ZnFe_2O_4$) solid solution series, EOS Trans. Amer. Geophys. Union 63 (1982) V41-40

7.   N. G. Lezhava, N. Sh. Dzagnidze, G. D. Chachanidze, Thermodynamic mixing parameters of $Ni_{1-x}Zn_xFe_2O_4$ solid solutions, Inorg. Mat. 23 (1987) 1399-1401

8.   S. E. Ziemniak, A. R. Gaddipati, P. C. Sander, Immiscibility in the $NiFe_2O_4$-$NiCr_2O_4$ spinel binary, J. Phys. Chem. Solids 66 (2005) 1112-1121

9.   L. K. Leung, B. J. Evans, A. H. Morrish, Low temperature Mössbauer study of a nickel-zinc ferrite: $Zn_xNi_{1-x}Fe_2O_4$, Phys. Rev. B 8 (1973) 29-43

10.   Yu. G. Chukalkin, V. R. Shtirts, Structure and magnetic properties of $Zn_xNi_{1-x}Fe_2O_4$ ferrites in structurally ordered and disordered states, Phys. Stat. Sol. A 160 (1997) 185-193

11.   T. Kanzaki, K. Kitayama, K. Shimokoshi, Mössbauer spectroscopy studies on Zn-bearing ferrite, J. Am. Ceram. Soc. 76 (1993) 1491-1494

12.   S. E. Ziemniak and R. A. Castelli, Immiscibility in the Fe_3O_4-$FeCr_2O_4$ spinel binary, J. Phys. Chem. Solids 64 (2003) 2081-2091

13.   L. Néel, Magnetic properties of ferrites: ferrimagnetism and antiferromagnetism, Ann. Phys. (Paris) 3 (1948) 137-198

14.   M. Temkin, Mixtures of fused salts as ionic solutions, Acta Physicochim. URSS 20 (1945) 411-420

15.   S. E. Ziemniak, L. M. Anovitz, R. A. Castelli, W. D. Porter, Magnetic contribution to heat capacity and entropy of nickel ferrite ($NiFe_2O_4$), submitted to J. Phys. Chem. Solids

16.   M. Hillert, M. Jarl, A model for alloying effects in ferromagnetic materials, CALPHAD 2 (1978) 227-238

17.   E. F. Westrum, D. M. Grimes, Low temperature heat capacity and thermodynamic properties of zinc ferrite, J. Phys. Chem. Solids 3 (1957) 44-49

18.   V. G. Vologin, Magnetic specific heat behavior near the antiferromagnetic-ferrimagnet phase transition in the lithium-zinc ferrite system, Sov. Phys. Solid State 31 (1989) 1856-60

19.   J. C. Ho, H. H. Hamdeh, Y. Y. Chen, S. H. Lin, Y. D. Rao, R. J. Willey, S. A. Oliver, Low-temperature calorimetric properties of zinc ferrite nanoparticles, Phys. Rev. B 52 (1995) 10122-26

20.   N. W. Grimes, On the specific heat of compounds with spinel structure. II. Zinc ferrite, a paramagnetic compound with magnetic ion occupying the octahedral site, Proc. Roy. Soc. Lond. A 338 (1974) 223-33

21. V. G. Vologin, S. F. Dubinin, Degenerate antiferromagnetic state in $ZnFe_2O_4$, Phys. Solid State 37 (1995) 1196-97

22. P. W. Anderson, Ordering and antiferromagnetism in ferrites, Phys. Rev. 102 (1956) 1008-1013

23. M. Tachiki, K. Yosida, Antiferromagnetism of Zn-ferrite, Prog. Theor. Phys. 17 (1957) 223-240

24. N. W. Grimes, A. J. Collett, Infrared absorption spectra of ferrites, Nature Phys. Sci. 230 (12 Apr 1971) 158

25. J. Preudhomme, P. Tarte, Infrared studies of spinels – III. The normal II-II spinels, Spectrochim. Acta 27A (1971) 1817-35

26. N. A. Landiya, V. S. Varazashvili, G. D. Chachanidze, Enthalpy and heat capacity of nickel-zinc ferrites between 25 and 1000°C, Izv. Akad. Nauk SSSR, Neorg. Mater. 5 (1969) 110-115

27. R. M. Persoons, E. DeGrave, P. M. A. deBakker, R. E. Vandenberghe, Mössbauer study of the high-temperature phase of Co-substituted magnetites, $Co_xFe_{3-x}O_4$. II. $x > 0.1$, Phys. Rev. B 47 (1993) 5894-5905

28. G. D. Chachanidze, N. G. Lezhava, Excess thermodynamic mixing parameters of the solid solution $Co_{1-x}Zn_xFe_2O_4$, Inorg. Mat. 23 (1987) 899-902

Table I
Summary of Test Conditions

Run. No.	LiCl/KCl molar ratio	Melting Point	Temp./Time
1	0/100*	800°C	1000°C/36 hr
2	30/70	620°C	700°C/1 mo
3	50/50	460°C	600°C/1 mo
4	60/40	350°C	500°C/3 mo
5	60/40	350°C	400°C/6 mo

* NaCl solvent used

Table II
XRD Characteristics of $(Ni_{1-n}Zn_n)Fe_2O_4$ Spinels Precipitated in Molten Salt

Run No.	Temp./Time Conditions	Spinel Characteristics			Stoichiometric Parameter, n**	n_2 (recalc.)***
		a_o, Å	fractional area	FWHM, deg		
1	1000°C/36 hr	8.3969 (1)	1.00	0.21	0.48	-
2	700°C/1 mo	8.400*	0.873	1.01	0.53	-
		8.365*	0.127	0.83	0.22	0.29
3	600°C/1 mo	8.414(1)	0.568	0.97	0.68 (0.64)	-
		8.369(1)	0.432	1.63	0.25 (0.17)	0.32
4	500°C/3 mo	8.423(1)	0.480	1.26	0.77 (0.75)	-
		8.362(1)	0.520	1.64	0.19 (0.10)	0.27
5	400°C/6 mo	8.427(1)	0.453	1.18	0.83 (0.80)	-
		8.351(1)	0.547	1.53	0.10 (0.0)	0.25

* Result for constrained deconvolution of [9, 3, 1], [8, 4, 4] and [10, 2, 0] peaks.
** Based on application of a_o result to Fig. 3. Revised estimate (enclosed in parentheses) accounts for presence of Fe(II) in spinel per dashed curve in Fig. 3; Fe(II)/Ni(II) ~ 0.28.
*** Calculation of n_2 by material balance from revised n_1 and spinel peak area ratio assuming complete reaction of starting material.

Table III
Microchemical Analyses of Solvus Phases in $(Ni_{1-n}Zn_n)Fe_2O_4$ Spinel Binary*

Run No.	Intercept at % Fe	Slope	Mean Composition of Ni-rich ferrite			Mean Composition of Zn-rich ferrite		
			at % Zn	at % Ni	at % Fe	at % Zn	at % Ni	at % Fe
1	-	-	17.1 (0.513)	15.4 (0.462) $n_1 = 0.53 \pm 0.05$	67.5 (0.024)			
2	67.91	0.67	9.5 (0.285)	22.4 (0.673) $n_1 = 0.30 \pm 0.09$	68.1 (0.042)	19.5 (0.584)	12.2 (0.367) $n_2 = 0.61 \pm 0.07$	68.3 (0.049)
3	72.45	-4.44		n.m.			n.m.	
4**	77.85	-9.61	2.5 (0.075)	18.8 (0.564) $n_1 = 0.12$	78.7 (0.361)	19.9 (0.597)	4.0 (0.120) $n_2 = 0.83$	76.1 (0.283)
5	79.22	-10.77	2.8 (0.083)	19.8 (0.594) $n_1 = 0.12 \pm 0.10$	77.4 (0.322)	22.3 (0.670)	6.6 (0.197) $n_2 = 0.77 \pm 0.11$	71.1 (0.134)

* Numbers in parentheses refer to stoichiometric coefficients x, y, z in spinel $(Zn_xNi_yFe_z)Fe_2O_4$.
** Solvus compositions determined from Fig. 6.

Table IV

Lattice Vibrational Contribution to Heat Capacity
of Trevorite and Franklinite*

Spinel	Infrared Peak Designation (cm^{-1})	Characteristic Temp.[c], K		Oct. Fe^{3+} Vibrational Anomaly via Eq. (13)	
		θ_E	θ_D	), K	g
NiFe$_2$O$_4$[a]	ν_1 (593)	853	--	199.4 ± 3.6	1.40 ± 0.03
	ν_2 (404)	--	581		
	ν_3 (330)	474.5	--		
	ν_4 (196)	--	282		
ZnFe$_2$O$_4$[a, b]	ν_1 (540)	776.5	--	195.5 ± 4.6	0.73 ± 0.03
	ν_2 (393)	--	565		
	ν_3 (325)	467.5	--		
	ν_4 (169)	--	243		

* Lattice contribution is defined by $C_V^{lattice}/R = 2E(\theta_1/T) + 2D(\theta_2/T) + 2E(\theta_3/T) + D(\theta_4/T)$ + Schottky "bump", where E and D are the respective dimensionless Einstein and Debye functions and the Schottky "bump", due to a vibrational anomaly in the Fe^{3+} octahedral ion, is calculated using Eq. (13).

a - Taken from Ref. [24], as revised by Ref. [20].

b - Ref. [25] gives alternate set of IR peaks for ZnFe$_2$O$_4$: 552, 425, 336 and 166 cm^{-1}.

c - $\theta_i = h\nu_i/k = 1.438 \nu_i$

Table V

Magnetic Contribution to Heat Capacity
of Trevorite and Franklinite

Ferrite	Eqns. Applied	Parameter Fitted	Temp. Range Fitted, K	C_P Correction Via Eq. (12)
$NiFe_2O_4$ (spin wave)[b] $s_A = 5/2$	Eq. (5)	$J_{AB}/k = 39.33 \pm 0.13$ K	53 - 1472	$\gamma_1 = 7.142 \pm 0.135 \times 10^{-5}$ $\gamma_2 = 4.216 \pm 0.091 \times 10^{-8}$
$s_B = 7/4$	Eq. (7)[a]	$a = 2.663 \ 10^{-6}$ $b = 1.065 \ 10^{-7}$		
$NiFe_2O_4$ (λ-transition)	Eqs. (10)	$K^- = 1.220 \pm 0.003$ $m = 7.185 \pm 0.052$ $K^+ = 1.489 \pm 0.007$ $n = 7.308 \pm 0.074$		
$ZnFe_2O_4$ (spin wave) $s_A =$ $s_B = 5/2$	Eq. (13)	$g = 0.275 \pm 0.080$ $) = 36.93 \pm 0.26$ K	4.6 - 345	$\gamma_1 = 7.363 \pm 1.487 \times 10^{-6 \ c}$ $\gamma_2 = 8.341 \pm 0.566 \times 10^{-8 \ c}$
$ZnFe_2O_4$ (λ-transition)	Eqs. (10)	$K^- = 0.498 \pm 0.015$ $m = 0.609 \pm 0.027$ $K^+ = 0.558 \pm 0.011$ $n = 7.584 \pm 0.555$		

a - Numerical integration results for $F(\omega_2)$ correlated vs. temperature via $F(\omega_2) = aT + bT^2$ ($R^2 > 0.998$).
b – Decay of spin wave contribution above T_C given by Eq. (10b), with $K^+ = 1.217$, $n = 102.00$ ($NiFe_2O_4$).
c – Correction calculated in Ref. [20] fitted to Eq. (11), see text.
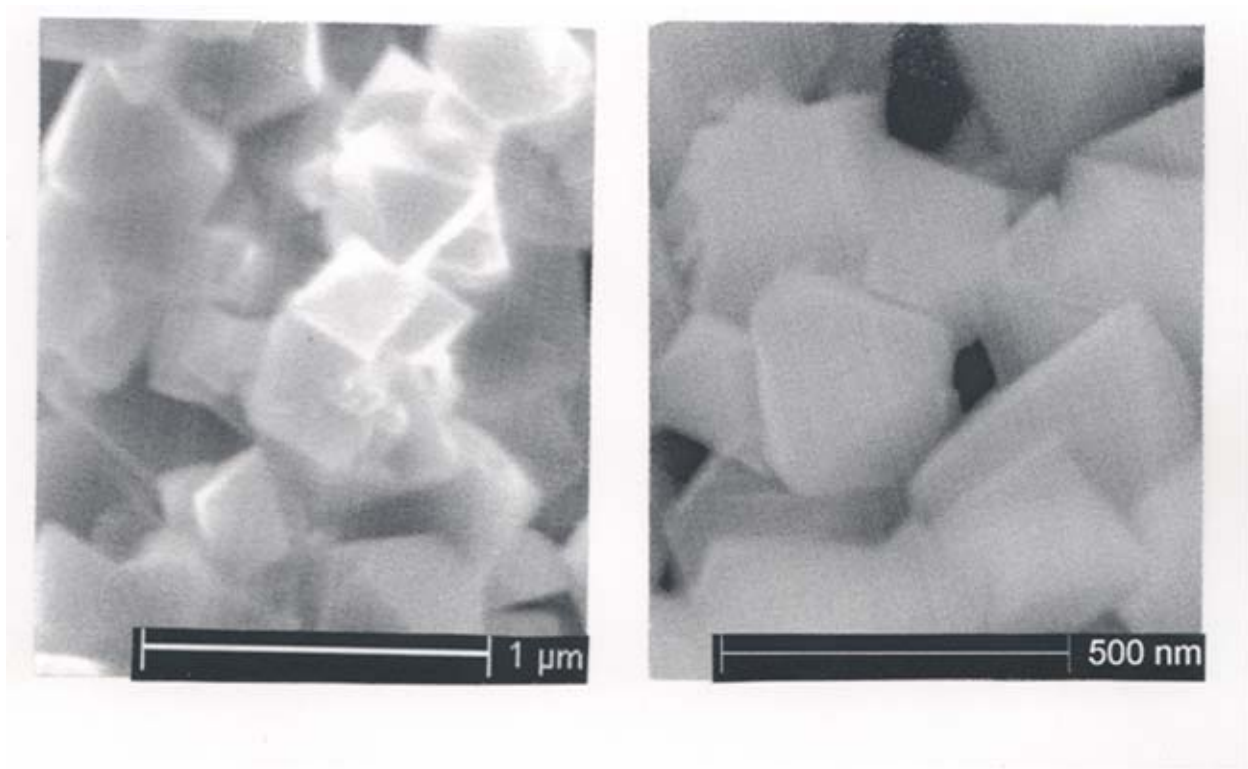
Fig. 1. SEM photographs of the $(Ni_{1-n}Zn_n)Fe_2O_4$ crystals formed in molten salt: (a) 400°C and (b) 500°C.
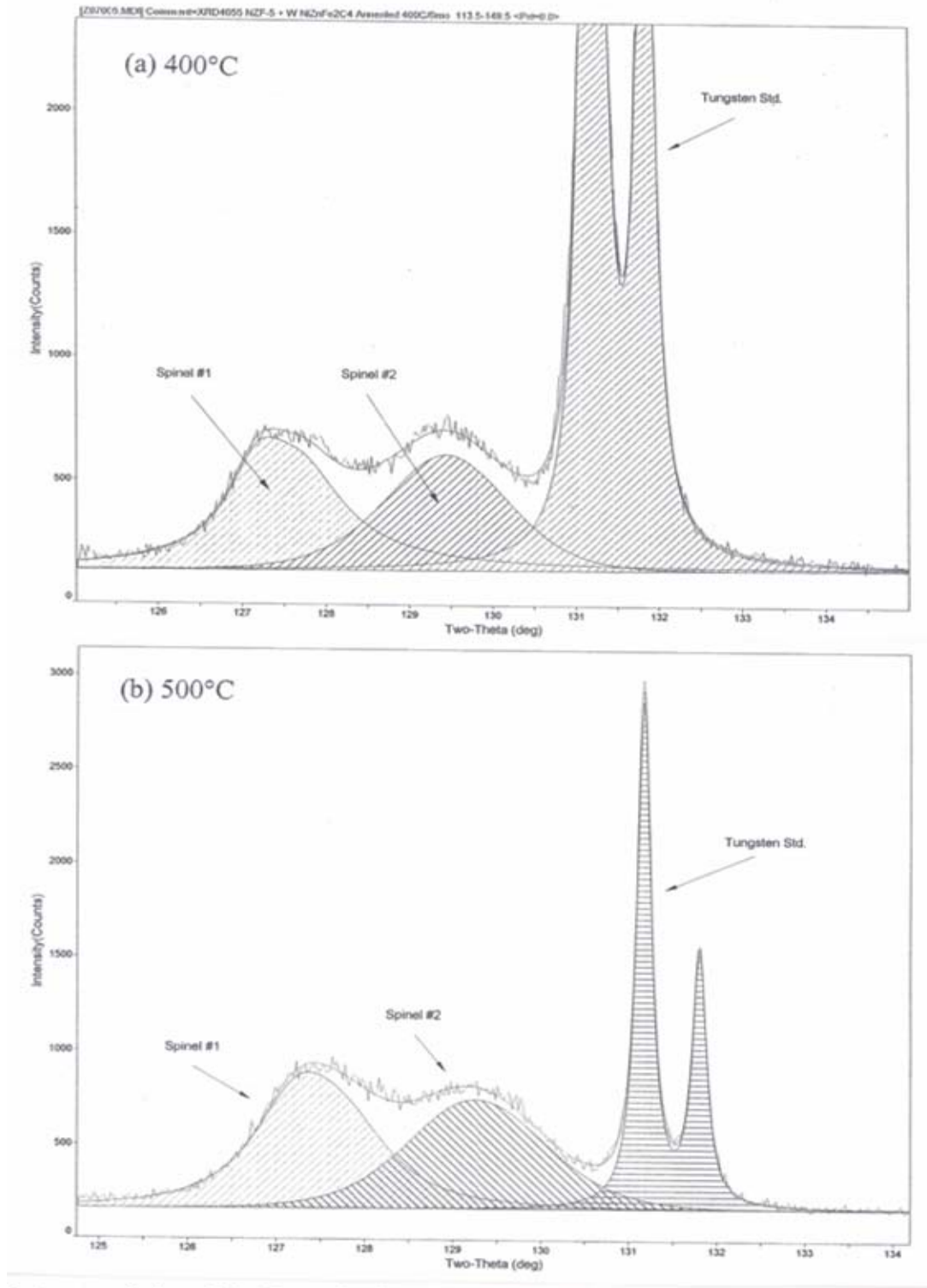
Fig. 2. Deconvolution of the [8, 4, 4] spinel XRD peak for 50/50 nickel/zinc ferrite mixtures precipitated in molten salt: (a) 400°C and (b) 500°C. The two highest peaks represent [3, 2, 1] reflections from the internal tungsten standard.
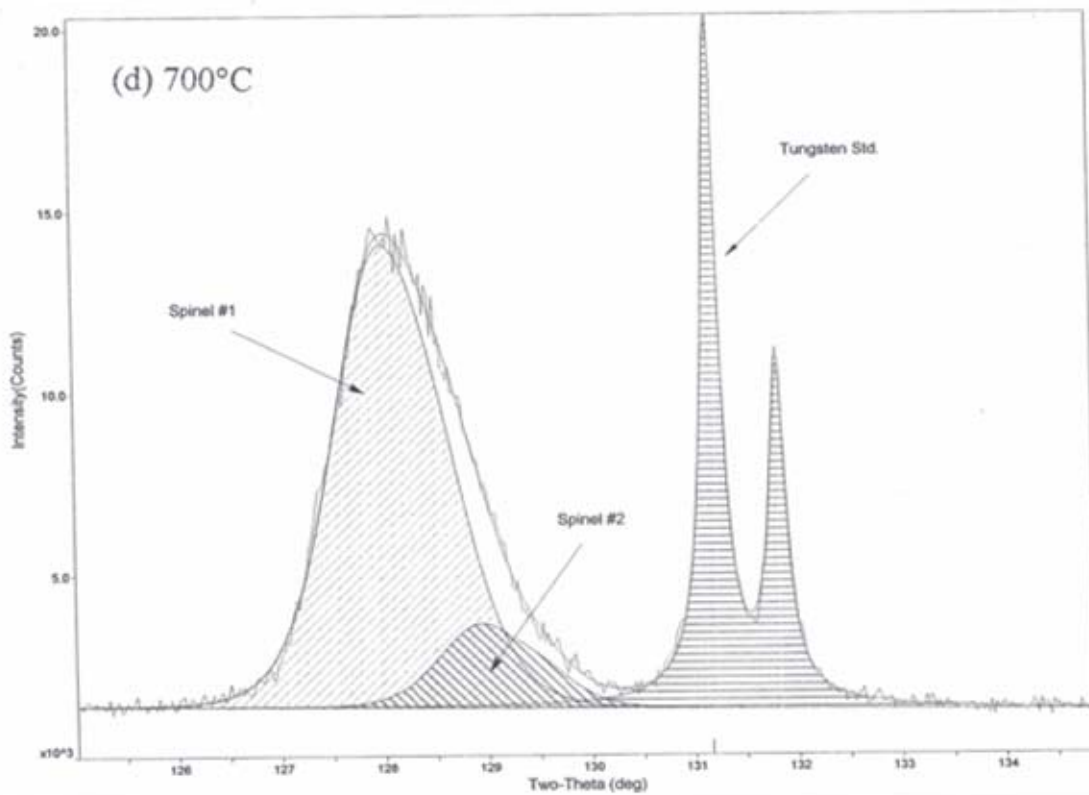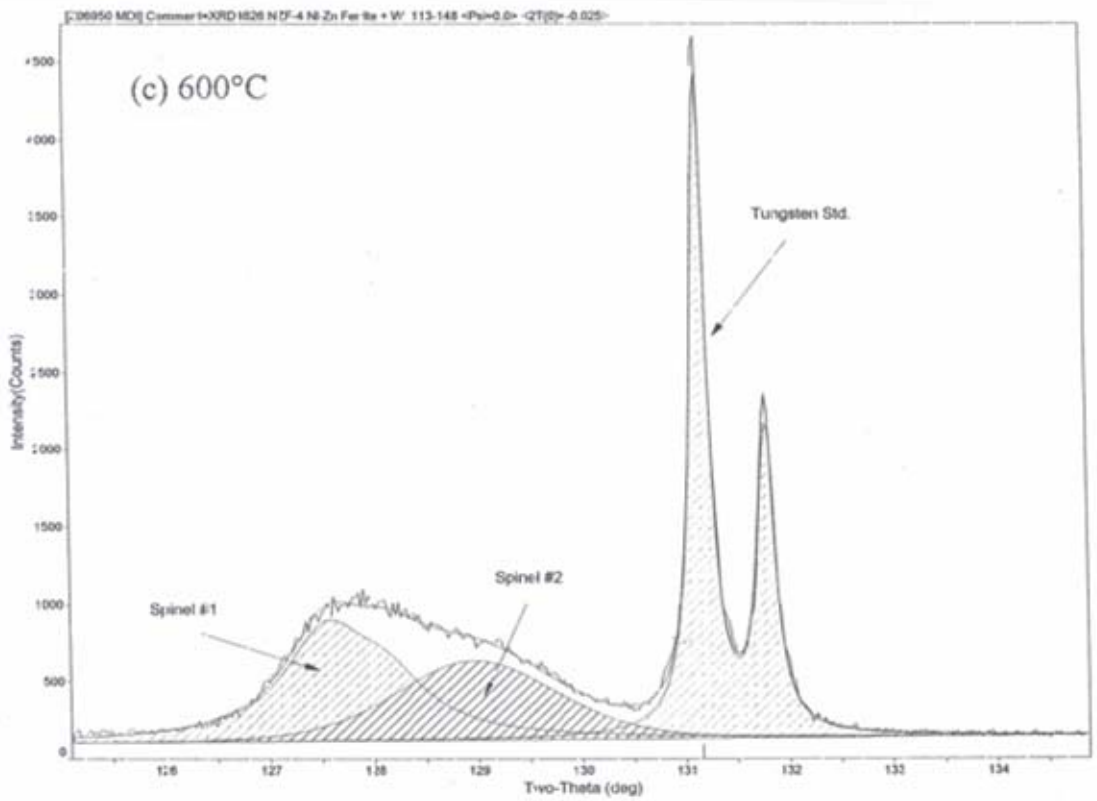
Fig. 2 (cont'd)   (c) 600°C and (d) 700°C.
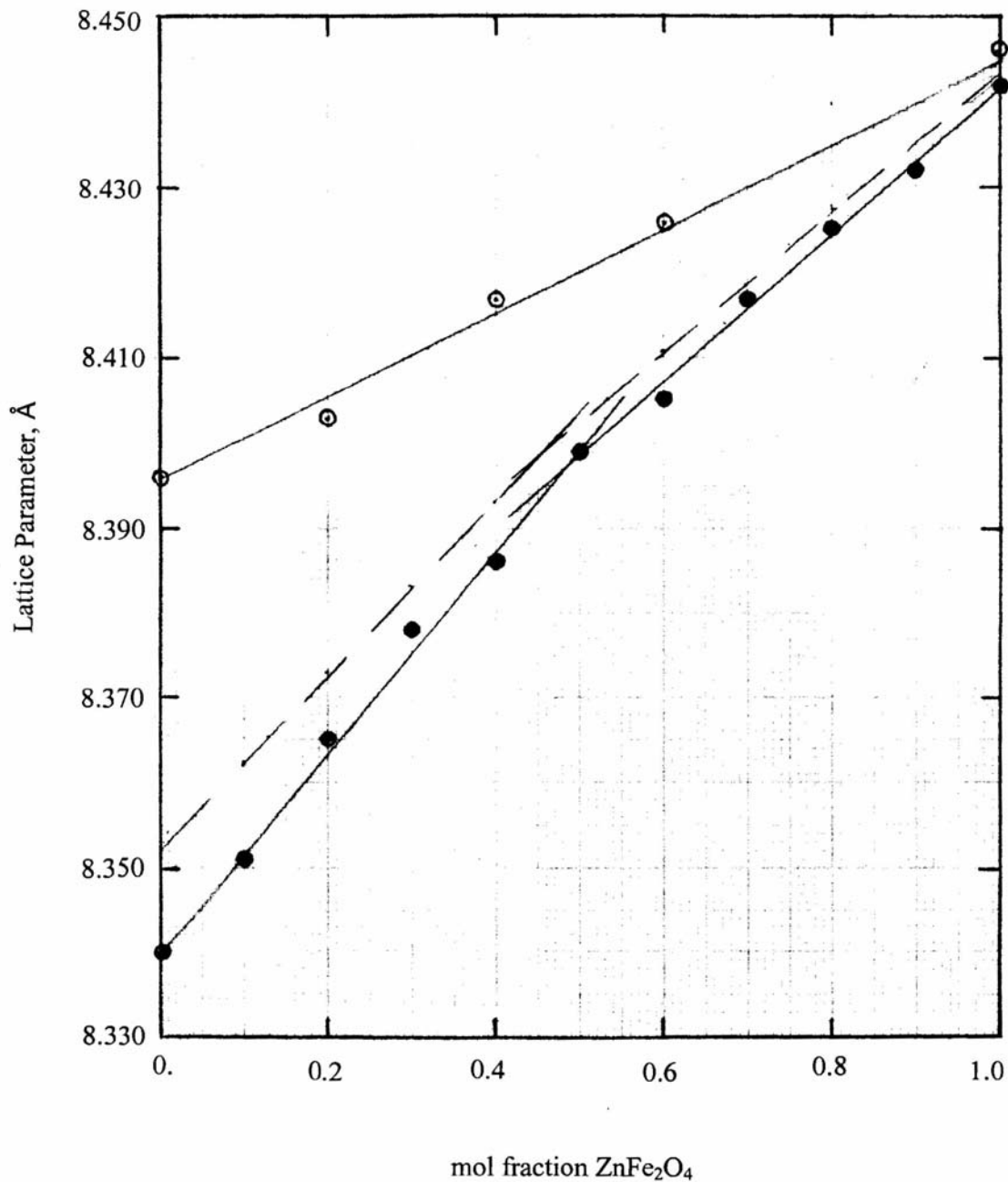
Fig. 3. Lattice parameters of single-phase spinel binaries: (a) $(Ni_{1-n}Zn_n)Fe_2O_4$ [9, 10], closed circles and (b) $(Fe_{1-n}Zn_n)Fe_2O_4$ [11], open circles. Dashed curve is estimate for $(Zn_xNi_yFe_z)Fe_2O_4$ with z/y = 0.28. Lattice parameters for the stoichiometric end member spinels are 8.339, 8.441 and 8.396 $\mathbf{C}$based on the recommended JCPDS file cards for trevorite (PDF# 10-325), franklinite (PDF# 22-1012) and magnetite (PDF# 19-629).
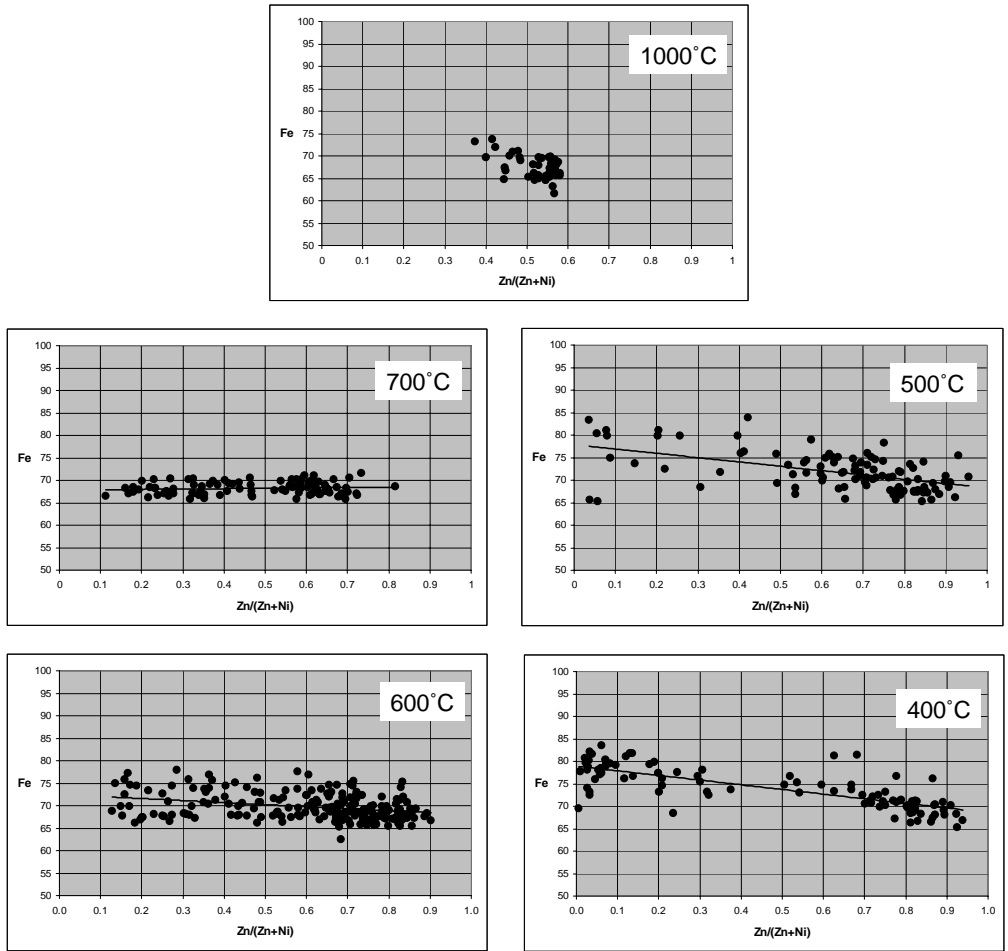
Fig. 4. AEM microchemical analyses (EDX) of individual spinel crystals synthesized during Runs 1-5.
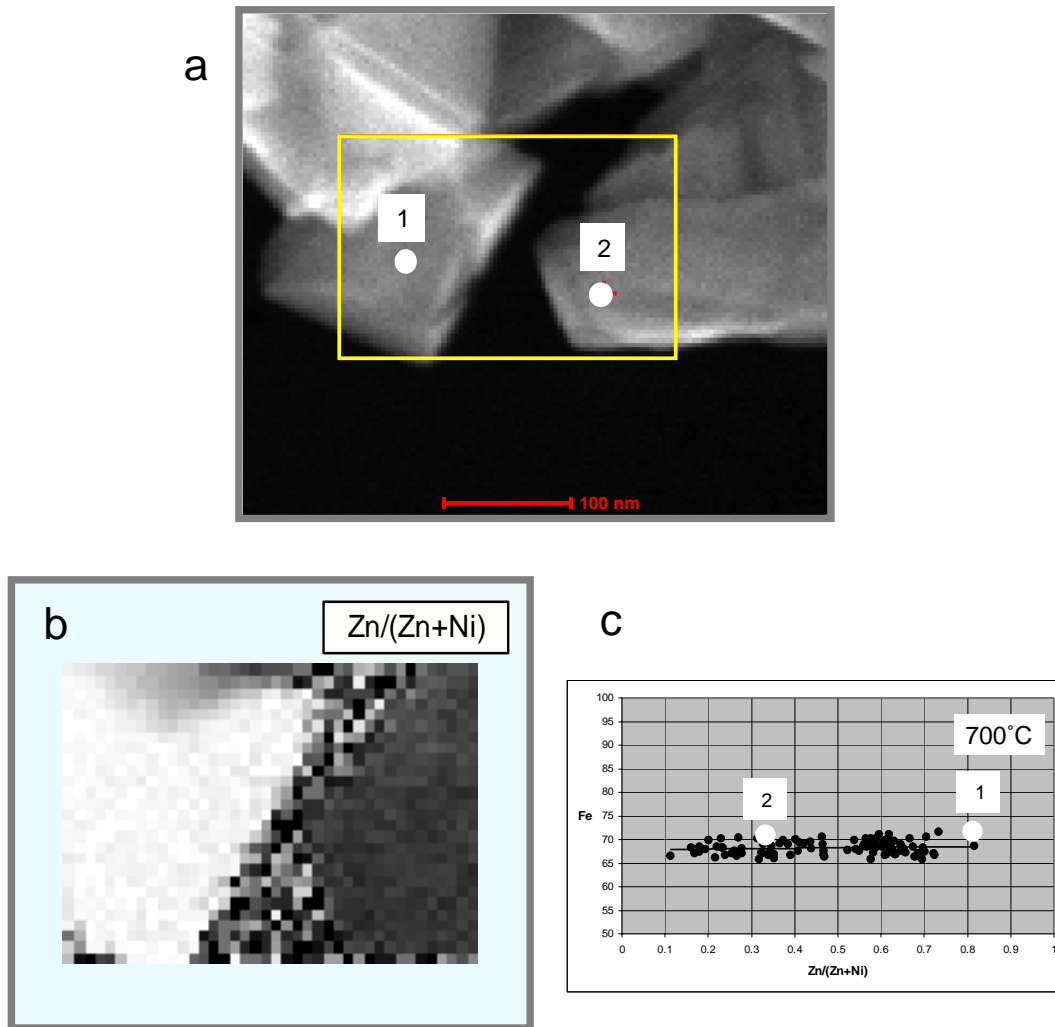
Fig. 5. (a) Secondary electron image of ferrite microcrystals synthesized at 700°C. Spots 1 and 2 are the approximate positions of pixel points showing high Zn and high Ni ferrite compositions, respectively, for the points plotted on the compositional diagram in (c). Figure (b) is a processed Zn/(Zn + Ni) ratio map obtained from the boxed area in (a). Spot 1 plots at the high end of the range, probably reflecting statistical variability because of the short counting time (2 s each) compared to about 180 s for the data points comprising the main plot.
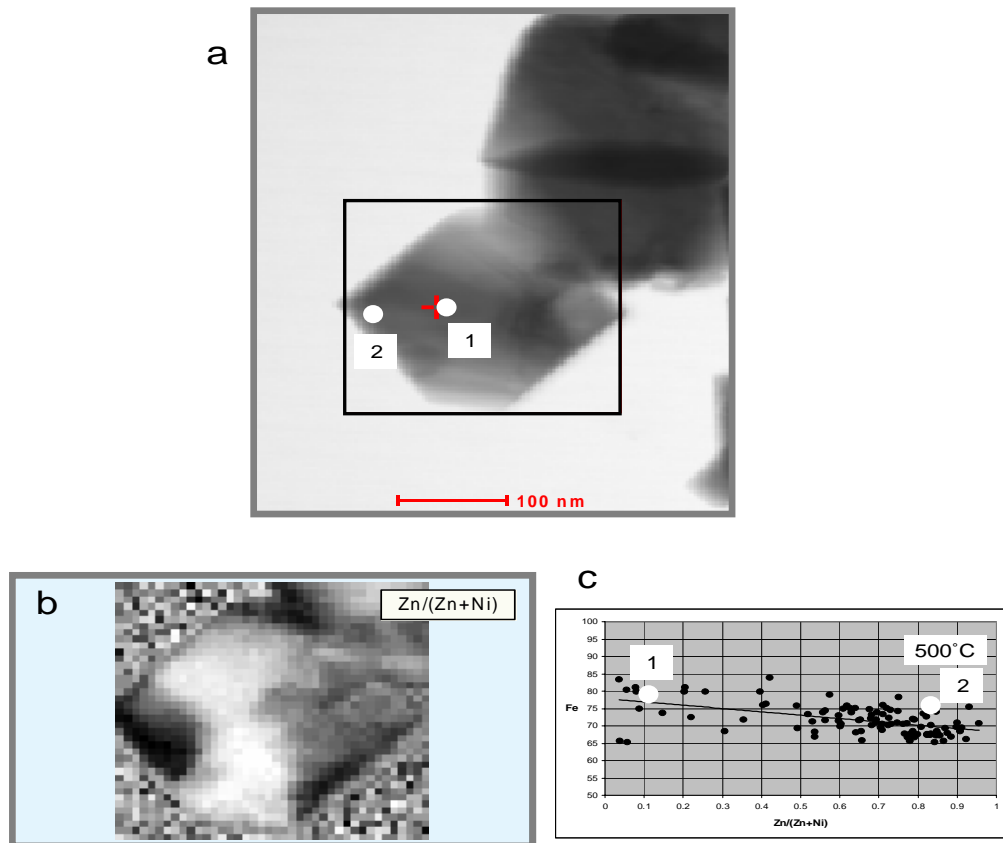
Fig. 6. (a) Bright field STEM image of ferrite microcrystal synthesized at 500°C. Spots 1 and 2 are the approximate positions of pixel points showing high Zn and Ni concentrations, respectively, for the points plotted on the compositional diagram in (c). In this case the two points represent compositions within the same crystal. Figure (b) is a processed Zn/(Zn + Ni) ratio map obtained from the boxed area in (a).
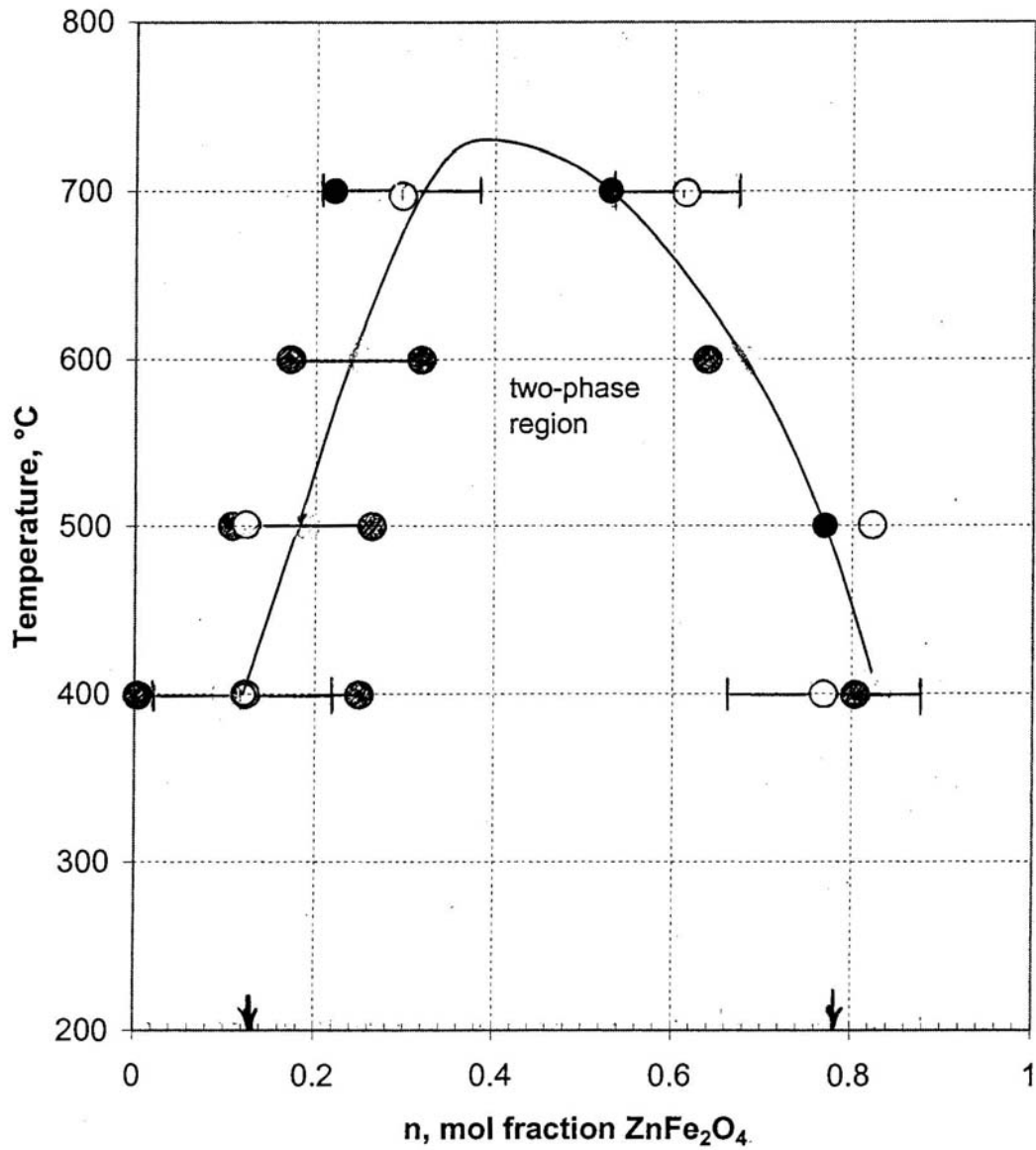
Fig. 7. Measured solvus in the $(Ni_{1-n}Zn_n)Fe_2O_4$ spinel binary. Compositions determined by XRD lattice parameters shown as closed circles; AEM microchemical analyses shown as open circles per Tables II and III, respectively. Arrows indicate predicted solvus at room temperature based on changes in configurational entropy and magnetic ordering entropy, per Fig. 15.
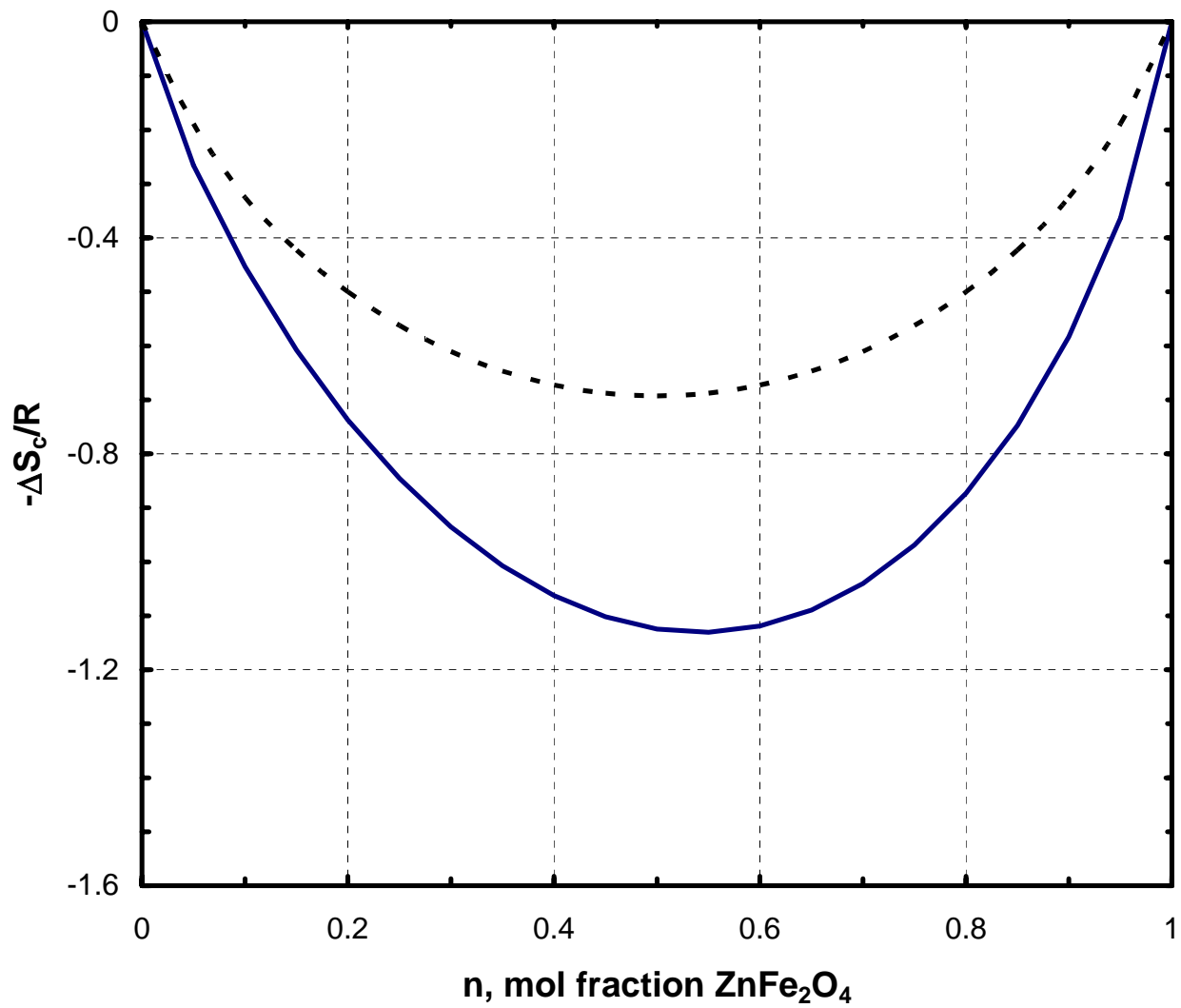
Fig. 8.   Entropy of mixing (∆ S$_{mix}$) based on changes in configurational entropy (∆ S$_c$) using cation distribution determined from M˙ssbauer and XRD results at room temperature. Ideal mixing formula shown as dashed line.
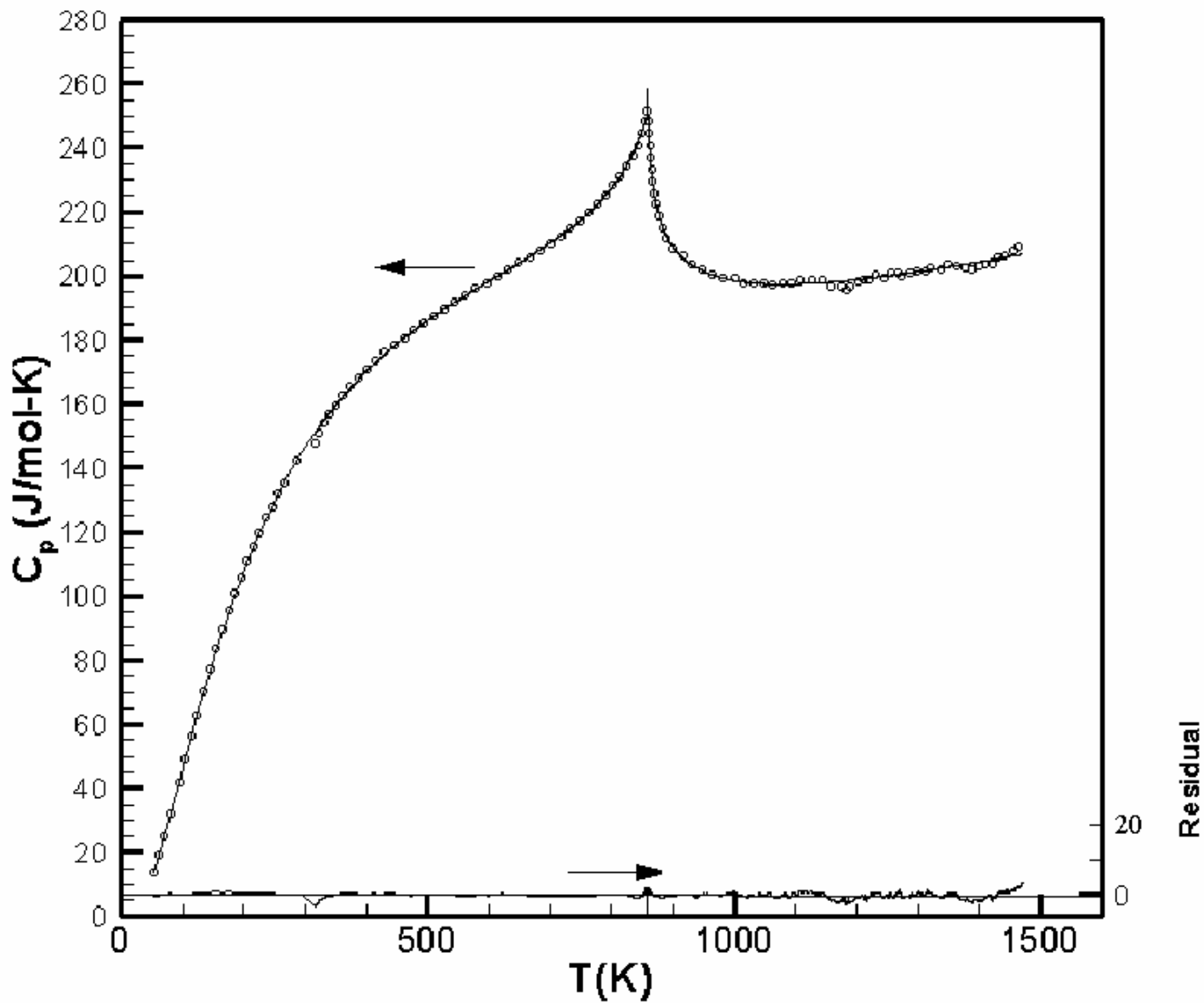
Fig. 9.   Comparison of measured and fitted heat capacities of nickel ferrite [15]. Residual is
            plotted along bottom axis of graph.
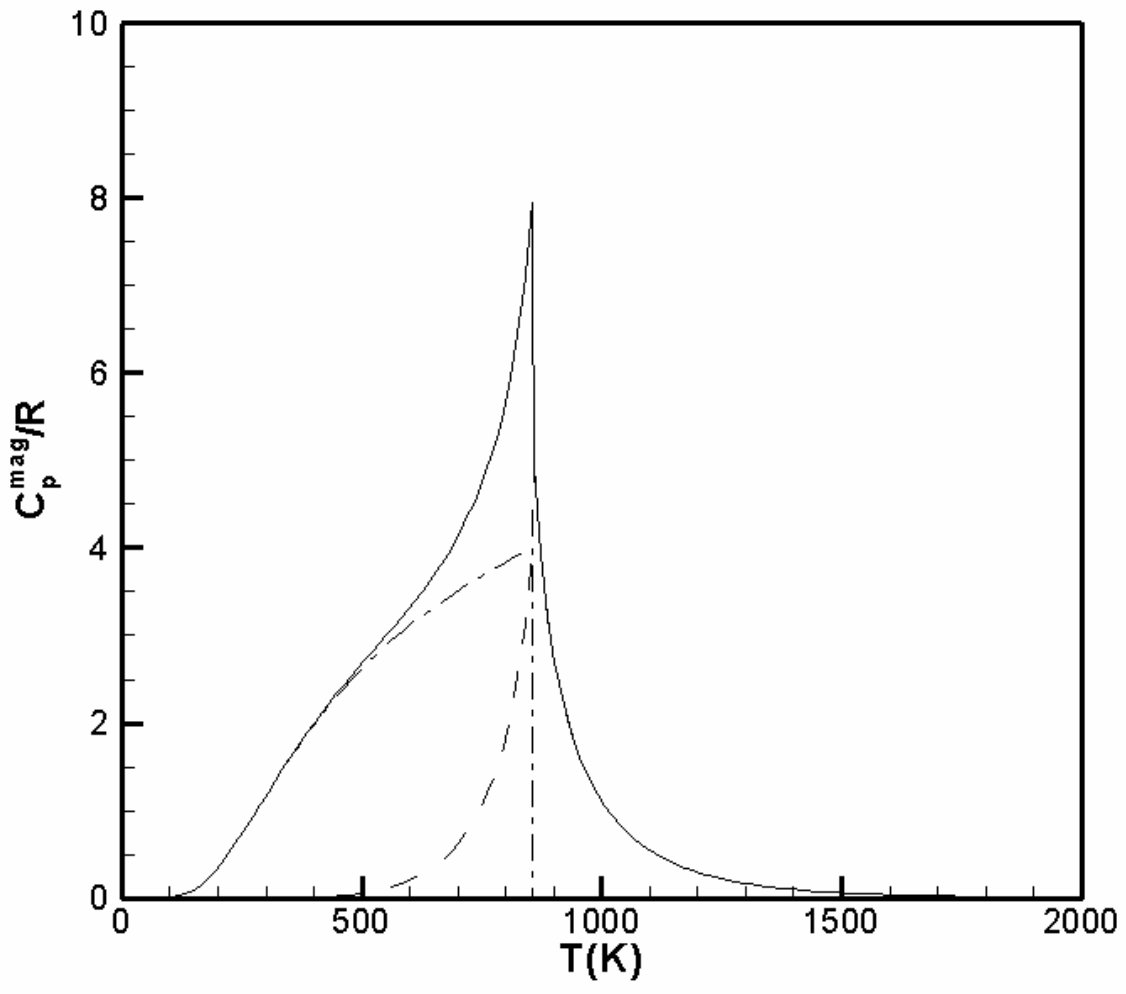
Fig. 10.   Magnetic contribution to heat capacity of nickel ferrite ($C_P^{mag.\ sw}/R + C_P^{mag,\ \lambda}/R$).
Long-short dashed line is spin wave contribution; dashed line is the Inden model.
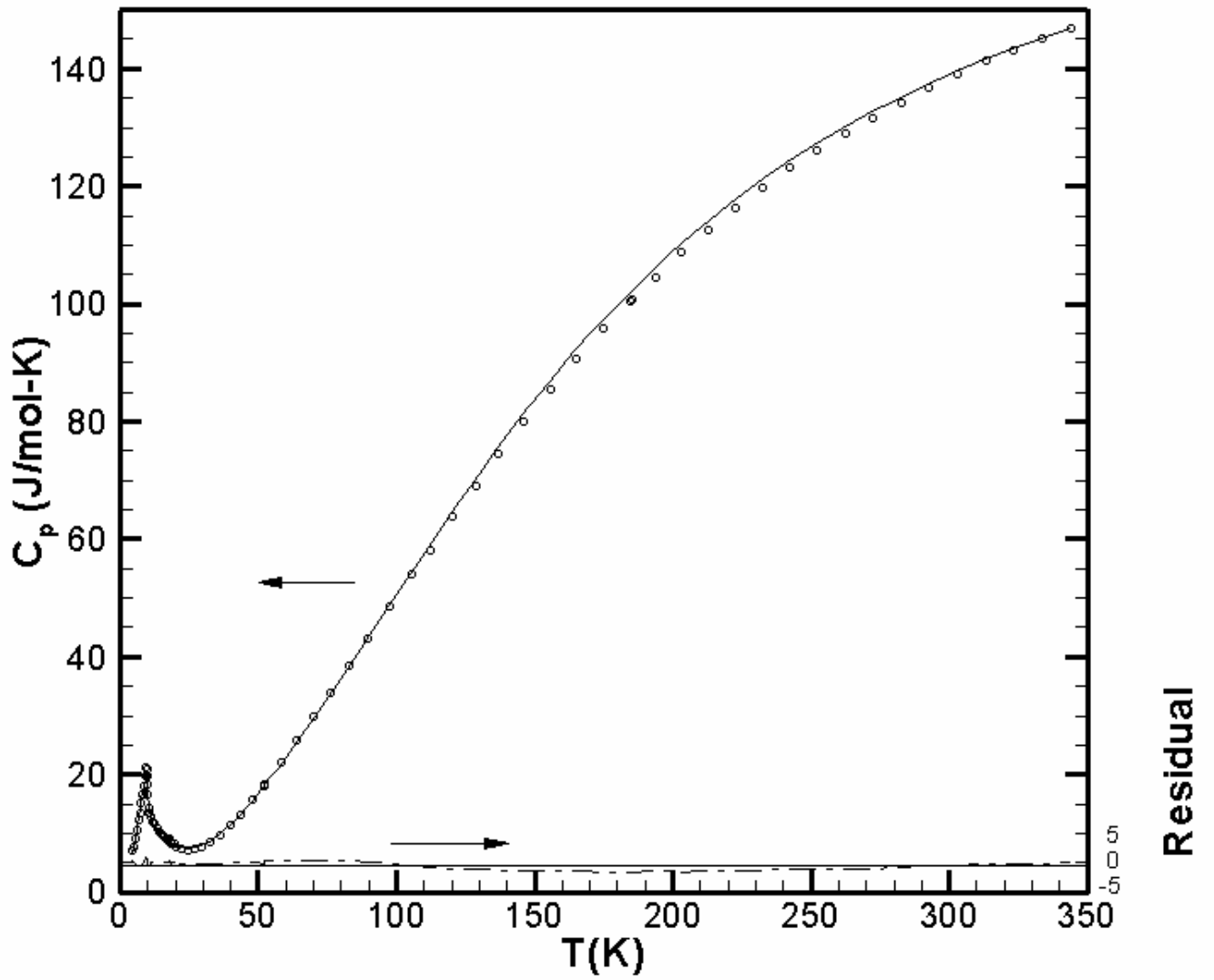
Fig. 11.   Calculated vs. experimental [17, 18] heat capacity of franklinite. Residual is plotted along bottom axis of graph.
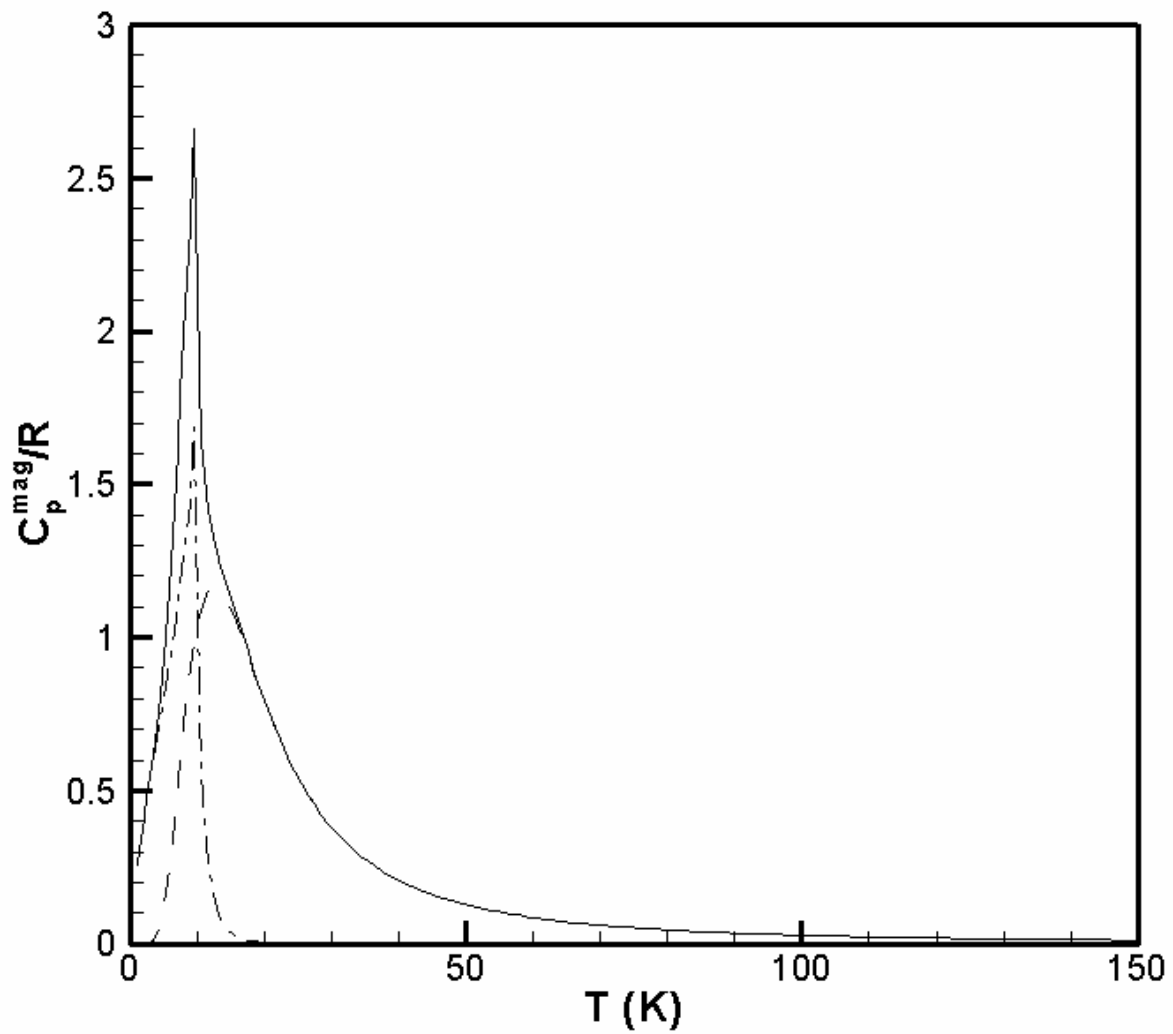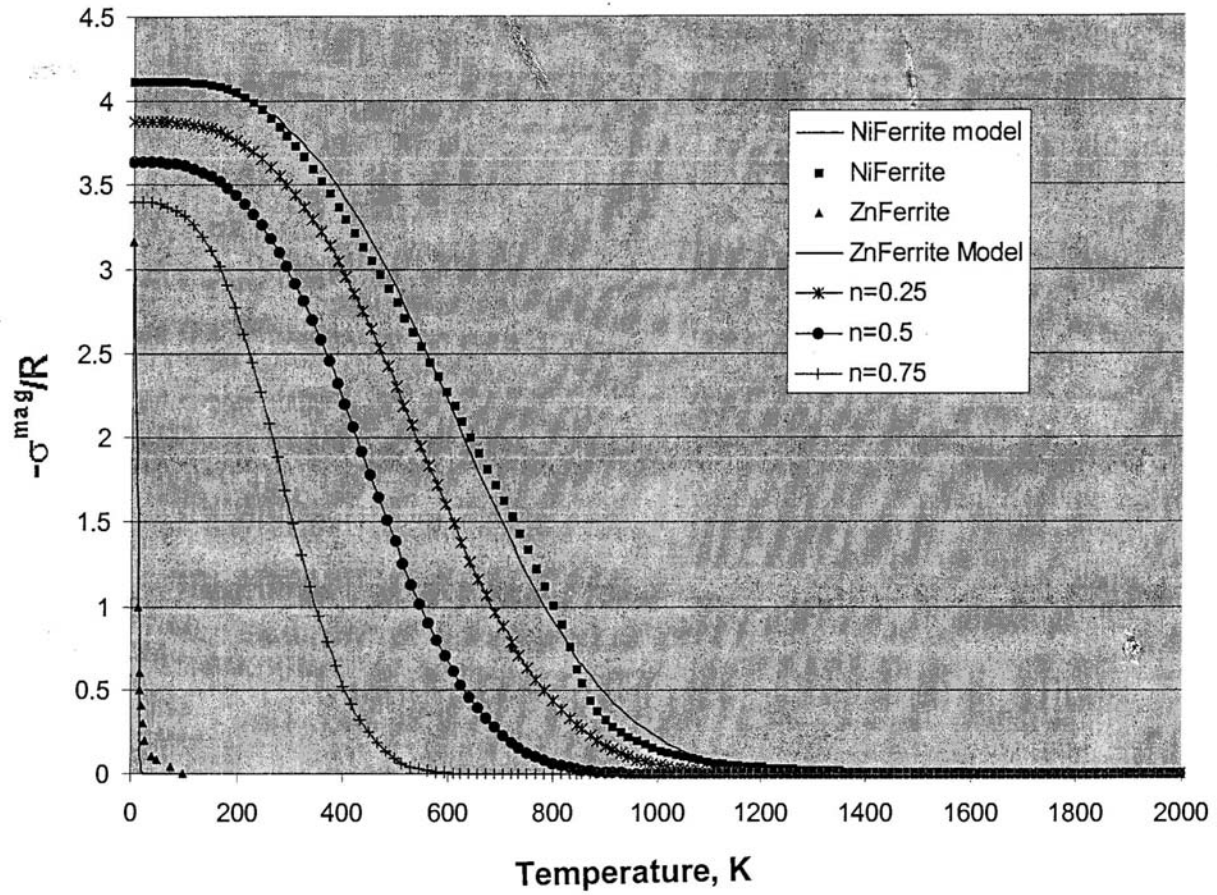
Fig. 12.   Magnetic contribution to heat capacity of zinc ferrite ($C_P^{mag.\ sw}/R + C_P^{mag,\ \lambda}/R$).
Long-short dashed line is spin wave contribution; dashed line is the Inden model.

Fig. 13. Magnetic ordering contribution to entropy, $\sigma^{mag}(T)$, for the $(Ni_{1-n}Zn_n)Fe_2O_4$ spinel binary according to Eq. (17). Curves for end-members ($n = 0$, 1) were obtained by integration of Figs. 10, 12, respectively, after division by temperature. Curves for intermediate n obtained from Eq. (17) with d_n and e_n interpolated as discussed in text.
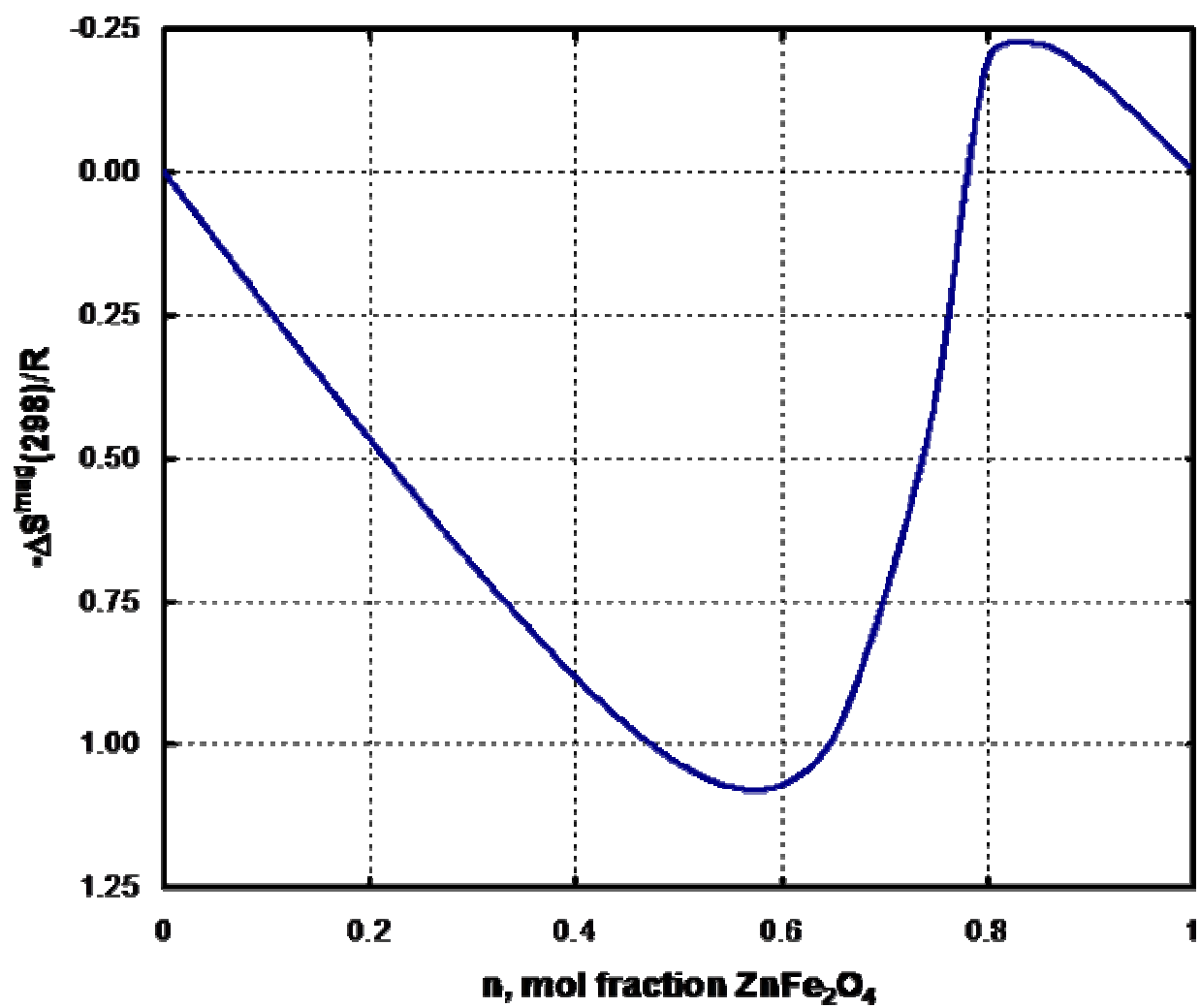
Fig. 14.   Magnetic ordering contribution to entropy of mixing in $NiFe_2O_4$-$ZnFe_2O_4$ binary at room temperature, per Eq. (20).
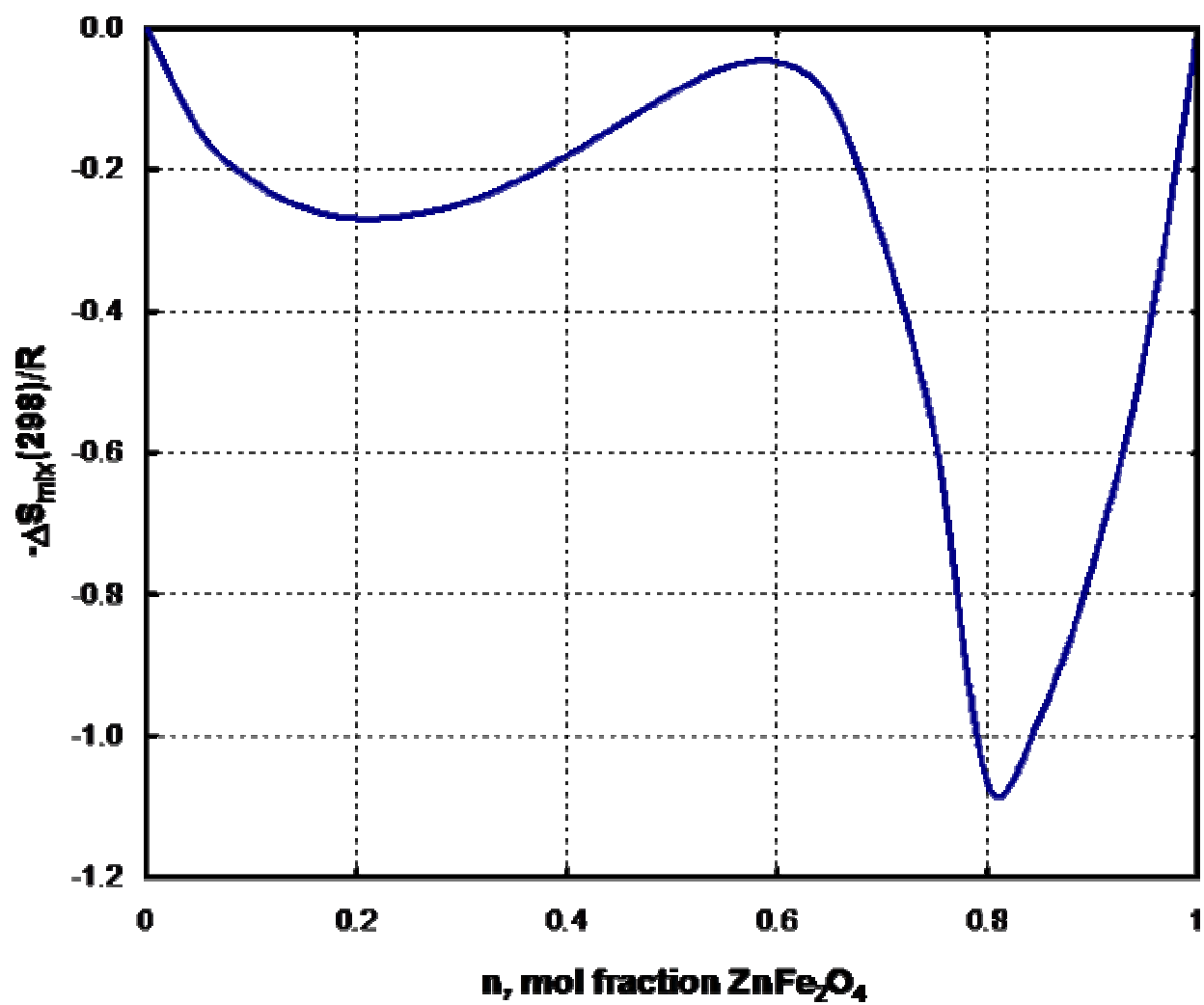
Fig. 15.   Entropy of mixing in $NiFe_2O_4$-$ZnFe_2O_4$ binary determined by summing contributions from changes in configurational entropy and magnetic ordering entropy.